Facilitating Reversible Cation Migration and Suppressing O_2 Escape for High Performance Li-rich Oxide Cathodes

Ke Chai, Jicheng Zhang, Qingyuan Li, Deniz Wong, Lirong Zheng, Christian Schulz, Maciej Bartkowiak, Dmitry Smirnov and Xiangfeng Liu**

Ke Chai, Jicheng Zhang, Qingyuan Li, Xiangfeng Liu
Center of Materials Science and Optoelectronics Engineering, College of Materials Science and Optoelectronic Technology, University of Chinese Academy of Sciences, Beijing 100049, P. R. China
E-mail: liuxf@ucas.ac.cn, zhangjc@ucas.ac.cn

Ke Chai, Xiangfeng Liu
Sino-Danish College, University of Chinese Academy of Sciences, Beijing, 100049, China

Deniz Wong, Christian Schulz, Maciej Bartkowiak, Dmitry Smirnov
Helmholtz-Zentrum Berlin für Materialien und Energie, Hahn-Meitner-Platz 1, D-14109, Berlin, Germany

Lirong Zheng
Beijing Synchrotron Radiation Facility, Institute of High Energy Physics, Chinese Academy of Sciences, Beijing 100049, China

Keywords: Li-rich oxides, oxygen escape, cation migration, oxygen redox, structural modification

High-capacity Li-rich Mn-based oxide cathodes show a great potential in next generation Li-ion batteries but suffer from some critical issues i.e. lattice oxygen escape, irreversible transition metal (TM) cation migration and voltage decay. Herein, we propose a comprehensive structural modulation in the bulk and surface of Li-rich cathodes through simultaneously introducing oxygen vacancies and P doping to mitigate these issues, and the improvement mechanism has

been revealed. First, oxygen vacancies and P doping elongates O-O distance, which lowers the energy barrier and enhances the reversible cation migration. Second, reversible cation migration elevates the discharge voltage, inhibits voltage decay and lattice oxygen escape by increasing the Li vacancy-TM antisite at charge and decreasing the trapped cations at discharge. Third, oxygen vacancies vary the lattice arrangement on surface from a layered lattice to a spinel phase, which deactivates oxygen redox and restrains O_2 escape. Fourth, P doping enhances the covalency between cations and anions and elevates lattice stability in bulk. The modulated Li-rich cathode exhibits a high-rate capability, a good cycling stability, a restrained voltage decay and an eleveated working voltage. This study presents insights into regulating oxygen redox by facilitating reversible cation migration and suppressing O_2 escape.

1. Introduction

Li-rich Mn-based oxides can deliver a capacity of about 300 mAh g^{-1} and have been emerged as one of the most competitive cathodes used for the next generation Li-ion batteries[1-5]. However, these oxides suffer from a big challenge of voltage decay, which is closely related to the issues of irreversible transition metal (TM) cation migration[6] and lattice oxygen escape[7-8]. It is generally accepted that the voltage fade is primarily rooted in the accumulation of irreversible cation migration. A comprehensive investigation of the Li-rich Mn-based oxide with an exacerbate voltage decline declares that an increasing amount of TM cations are indeed trapped into the Li layers[9,10]. Some studies identify that the structure of Li-rich Mn-based oxides gradually changes from a layered lattice to a spinel phase with the accumulation of irreversible cation migration[11,12]. However, TM_{Li}-V_{TM} (V: vacancy) antisite, which is caused by the cation migration from TM layer to Li layer[13], thermodynamically stabilizes the oxidized lattice oxygen product of O-O dimer[14]. Moreover, lattice oxygen escape accelerates the irreversible cation migration and structural phase transition[15]. It is confirmed that the undesirable structural degeneration starts from the surface to the bulk for Li-rich Mn-based oxides[16,17]. One recent study declares that localized O_2 acts as the oxidation product of lattice oxygen[18]. Compared with the material bulk, O_2 first escapes from the surface, thus exacerbating the lattice destruction of the material surface[19]. Therefore, how to enable an reversible cation migration in the bulk phase as well as inhibit the lattice oxygen escape in the surface is highly important for Li-rich cathodes.

Some progresses have been made in improving the reversible cation migration and inhibiting lattice oxygen escape[20,21]. Kang et al. reported that O2 phase Li-rich oxides prepared by an ion exchange method showed an enhnced reversible cation migration[21]. Surface treatment is another way to inhibit lattice oxygen escape[22-29]. Oxygen vacancies have been proved to inhibit voltage decay and lattice oxygen escape in some studies[30,31]. Nakamura et al. found that the oxygen-deficient materials exhibited a greater hysteresis voltage than the bare sample due to a facilitated cation migration[30]. But the underlying mechanism still needs to be further clarified.

In this study, we propose a feasible strategy to simultaneously tune the bulk and surface structure of Li-rich oxides through introducing oxygen vacancies and P doping, and the irreversible cation migration and lattice oxygen escape are largely alleviated. Combined with spectroscopy, diffraction, micrography, and theoretical calculations, the intrinsic mechanism is revealed. On the one hand, the elongated O-O distance in the bulk caused by oxygen vacancy (Vo) and P doping reduce the steric hindrance, which lowers the energy barrier of cation migration between TM site and Li site. This elevates the discharge voltage and inhibits voltage decay and lattice oxygen escape by increasing the TM_{Li}-V_{TM} antisite at charge and decreasing the trapped cations at discharge. On the other hand, P doing elevates lattice framework stability by enhancing the covalency between cations and anions. A spinel-like passivated surface deactivates the oxygen redox and restrains the O_2 escape. The optimized cathode material exhibits an improved cycling stability (98.8% *VS* 85.8% @ 200 cycles), an elevated discharge voltage (3.512V *VS* 3.387V @ 1C), a restrained voltage decay rate (0.028% *VS* 0.041% per cycle) and a relieved lattice oxygen escape (0.10μmol mg^{-1} VS 0.27μmol mg^{-1} @ 1st cycle). This study proposes a new strategy of reducing the steric hindrance for facilitating reversible cation migration and a comprehensive modification involving both bulk and surface, which presents some insights into designing anionic redox-active cathode materials with high performances.

2. Results and Discussion

2.1. Structural characteristics of materials

A representative cobalt-free Li-rich Mn-based oxide ($Li_{1.2}Mn_{0.6}Ni_{0.2}O_2$, labeled as LMNO) was selected for this study. To compare the synergistic improvements of Vo and P doping, we prepared the comparison sample (LMNO), surface treated sample (LMNO-V_O), P doping sample (LMNPO) and synergic treatment sample (LMNPO-V_O), respectively. The material synthesis design is as follows. Vo in the surface of the oxide is introduced by soaking the Li-

rich oxides into hydrazine hydrate, and P doping is fulfilled by introducing P element into the precursor. Since P and O have a close electronegativity (O:3.44, P:2.19), the introduction of P[32-34] can enhance the covalency between cations and anions, thus making up for the instability caused by oxygen defects. The existences of V_O and P doping in LMNPO-V_O could be probed from electron paramagnetic resonance (EPR) in Figure S1 and X-ray photoelectron spectroscopy (XPS) in Figure S2. Due to the presence of V_O and P, there are some differences between LMNPO-V_O and LMNO in the valence states of Ni and Mn, evidenced by the peak shifts in Ni/Mn XPS spectra (Figure S2). XPS combined with Ar^+ etching XPS and time-of-flight secondary ion mass spectrometry (TOF-SIMS) demonstrate that compared with the surface, P doping in the bulk is reduced (Figure S3). According to the ionic radius of P and Raman results (Figure S4), P might exist in the tetrahedron site. X-ray diffraction (XRD) patterns of four prepared samples in Figure S5 all conform to the structure of Li-rich Mn-based oxides.

The Rietveld refinements of the neutron diffraction (ND) provide the structural details (Figure 1a, 1b, Figure S6, Table S1, S2). It verifies the existence of V_O in LMNO-V_O and LMNPO-V_O. The contents of V_O in LMNPO-V_O obtained by ND refinement are both close to 2%. Moreover, the ND refinements demonstrate that P doping and Vo have obvious effects on the lattice position of oxygen anions, which directly affects the thickness of TMO_2 slab ($S_{(TMO2)}$) and LiO_2 interslab ($I_{(LiO2)}$). For refining P, we first assigned the value to the P content by the inventory ratio at the beginning of refinement, and then refined its site occupation. Compared with LMNO, the bond lengths of O-O and TM-O for the modified samples have varying degrees of elongation. The elongation can demonstrate the enlargement of the octahedral in size and decrease the electrostatic repulsive force between the Li ion and the TM ion when the Li ion is hopping across the intermediate tetrahedral site.

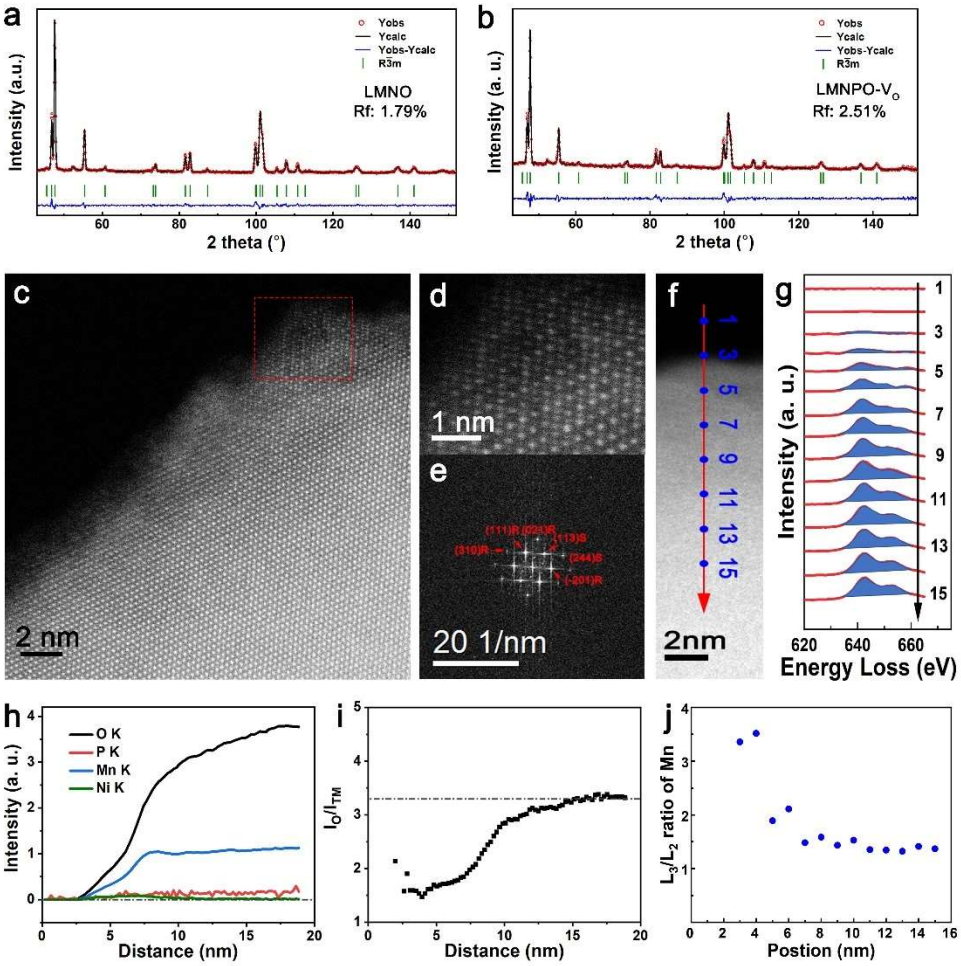

Figure 1. Powder ND refinement patterns of LMNO (a) and LMNPO-V_O (b). (c) AC-STEM image of the LMNPO-V_O sample. The enlarged image (d) and the SAED pattern (e) of the sample in the selected area of Figure 1c. R represents rhombus, S stands for spinel. (f) STEM area for line scanning pathway of EEL spectra. (g) the Mn $L_{2,3}$-edges EELS obtained from the locations indicated by the dots in f. (h) Distribution analysis of elements corresponded with line scanning pathway. (i) The calculated atomic ratios of O/Mn. (j) The Mn L_3/L_2 intensity ratio calculated from Figure 1g.

Scanning electron microscopy (SEM) images in Figure S7 declare that four samples have a similar particle size and morphology. Transmission electron microscopy (TEM) images (Figure S8) display the structural details of the samples. The energy dispersion spectra (EDS) mappings show a uniform element distribution for all samples and confirm the existence of P element in LMNPO and LMNPO-V_O. The fast Fourier transform (FFT) and the TEM images in high magnification show that in LMNPO-V_O and LMNPO-V_O, after treating with hydrazine hydrate, atoms on the surface of the particles underwent atomic rearrangement to produce spinel-like substances. While the bulk domain of LMNPO-V_O still accords with the atomic

arrangement of Li-rich layered oxides, which is verified by selected-area electron diffraction (SAED).

Figure 1c shows the spherical aberration-corrected scanning transmission electron microscopy (AC-STEM) image of the LMNPO-V_O sample, while the enlarged image and SAED pattern are provided in Figure 1d, 1e, respectively. The Bragg reflections for Li_2MnO_3 and spinel-like structure are indexed in Figure 1e. Meanwhile, a set of electron energy loss spectroscopy (EELS) spectra are obtained from the surface to the bulk of LMNPO-V_O, of which the line scanning pathway is shown in Figure 1f. The Mn L-edge and O K-edge EELS are simultaneously recorded in Figure 1g and Figure S9. In Figure 1h, the distribution analysis of elements corresponded with line scanning pathway indicate that there exists a heterostructure with a thickness of 5 nm. The atomic ratios of O/Mn in Figure 1i calculated from Figure 1h demonstrates the existence of V_O in the particle surface. Figure 1j displays a deeper view of the Mn EELS by testing the L_3/L_2 ratio of Mn $L_{2,3}$ edges, which are sensitive to Mn valence[35]. The L_3/L_2 ratio in the range of 3-5 nm is larger than that in the range of 6-15 nm, indicating a lower valence of Mn in the surface spinel structure with a 5 nm-thick shell than that in the bulk layered phase.

2.2. Electrochemical performances

The shapes and coulomb efficiencies of initial charge-discharge curves indicate different redox behaviors in LMNO and LMNPO-V_O (Figure S10). The normalized second-cycle charge-discharge curve at 0.05 C shows larger voltage hysteresis for LMNPO-V_O than LMNO (Figure 2a). This indicates that the energy efficiency, which is defined by the ratio of the discharge energy to charge energy, can be lower than the bare sample. The larger voltage hysteresis is because LMNPO-V_O has more migrated cations at charging. But it should be noted that these cations can be reversibly migrated back, which will be elaborated and proved in detail later. Figure 2b declares that the rate performance of LMNPO-V_O is improved. Galvanostatic intermittent titration technique (GITT) in Figure S11 declared the Li^+ diffusion in LMNPO-V_O is quicker than LMNO.

The cycling performances of LMNO and LMNPO-V_O at 0.2 C are presented in Figure 2c. The charge-discharge curves (Figure S12) and dQ/dV curves (Figure 2d, 2e) reflect the details of the electrochemical evolution of the materials with cycling. According to previous study[36], the capacity can be roughly divided into three parts: O contribution at high potentials, Ni contribution at medium potentials, and O/Mn contribution at low potentials, which just correspond to the three pairs of redox peaks in Figure 2d and 2e. With cycling, for LMNO, the

Ni contribution decreases obviously, the redox behaviors of O and O/Mn also change obviously, whereas LMNPO-V_O does good in inhibiting these declines. It is found in the plots of corresponding discharge capacity contribution that, with cycling, the O/Mn activity of LMNPO-V_O is increasing, the Ni activity is basically unchanged. While for LMNO, the O/Mn activity is slightly declining, accompanied by a sharp decrease in Ni activity (Figure 2f). These improvements can be attributed to reversible cationic/anionic redox due to reversible cation migration and inhibited lattice oxygen escape, which will be well evidenced in the following. Figure S13 declares, the voltage decay of LMNPO-V_O is suppressed. At the same time, the hysteresis voltage of LMNPO-V_O is more stable than that of LMNO, indicating a restrained structure damage.

As shown in Figure 2g, LMNPO-V_O retains a specific capacity of 163 mAh g^{-1} and a capacity retention of 98.8 % after 200 cycles at 1 C. In contrast for LMNO, it only delivers 121 mAh g^{-1} and a capacity retention of 85.8 % after 200 cycles. The voltage decay rate is reduced from 0.041% for LMNO to 0.028% for LMNPO-V_O. The charge-discharge plots and corresponding dQ/dV curves in Figure S14 and S15 could also reflect the remarkable improvement of LMNPO-V_O on suppressing voltage decay. From these curves, it is clear that compared with other three materials, LMNPO-V_O can maintain both capacity and redox activities. The specific energies at 1 C during cycles are ploted in Figure 2h. The specific energy maintenance has been largely increased from 75.6% for LMNO to 95.1% for LMNPO-V_O. As for the performances at 5 C, LMNPO-V_O has a high capacity retention of 92.2 % after 400 cycles at 5 C, while it is only 84.0 % for LMNO (Figure S16). The comparison of electrochemical performances for LMNPO-V_O and other examples in published works is listed in Table S3.

Figure S17 present the EIS plots and relationships of Z' and $\omega^{-1/2}$ from EIS plots of all the samples before and after cycling. The Warburg constant (σ) could be tested by the relationships of Z' and $\omega^{-1/2}$ and Li-ion diffusion coefficients (D_{Li}) of LMNO and LMNPO-V_O samples are 1.26×10^{-14} and 3.10×10^{-14} cm^2 s^{-1}, respectively, and those of LMNO and LMNPO-V_O after cycles are 6.10×10^{-15} and 1.48×10^{-14} cm^2 s^{-1}, respectively, indicating the LMNPO-V_O has a better Li-ion conductivity. In addition, in the EIS plots of four materials, LMNPO-V_O has the smallest charge transfer resistance, which may be due to the high electronic conductivity.

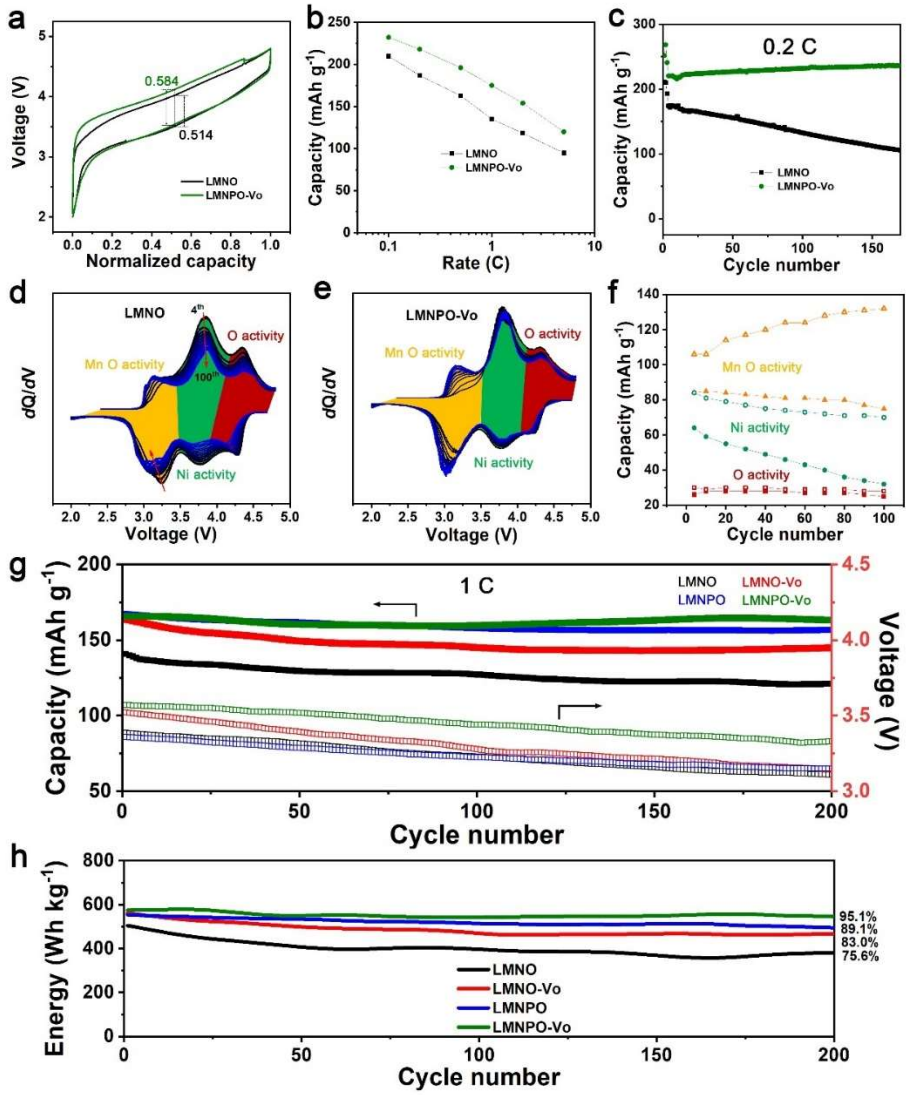

Figure 2. (a) The normalized charge-discharged plots in the second cycle at 0.05C. (b) The rate performances. (c) The cyclic performance at 0.2 C. The dQ/dV plots of the charge-discharge curves from 4th to 100th for LMNO (d) and LMNPO-V_O (e) at 0.2 C. (f) The comparison of capacity contribution of O, Ni, O/Mn in LMNO and LMNPO-V_O at different cycle numbers at 0.2 C. (g) The specific discharge capacity and average discharge voltage versus cycle number at 1C. (h) The specific energy versus cycle number at 1C.

2.3. Reversible cation migration

The in situ XRD patterns of LMNO and LMNPO-V_O are shown in Figure S18 and Figure 3a, respectively. Upon delithiating, for both materials, the (003) peak shifts to lower angle while the (101) and (104) peaks shift to higher angle, demonstrating the extended c parameter and reduced a parameter. The c expansion is attributed to the enhancement of the electrostatic repulsion between adjacent oxygen layers with Li^+ extraction from the Li^+ layers[37,38].

Compared with LMNO, the shifting of the XRD peaks for LMNPO-V_O is relieved. The moving span of (003) peak for LMNPO-V_O is between 18.13° and 18. 21°, while it is between 18.26° and 18. 42° for LMNO. The evolutions in parameter a, c and cell volume of LMNO and LMNPO-V_O upon charging and discharging stem from the refined in situ XRD data are plotted in Figure 3b. Two samples show a similar varying trend for the structural parameters, but the changes of the cell parameters of LMNPO-V_O are smaller than that of the LMNO. Compared with the XRD plot for pristine state, the 003 peak of LMNO largely decreases after 1 cycle, while this phenomenon is obviously relieved for LMNPO-V_O, indicating that the structural reversibility of LMNPO-V_O is better than LMNO (Figure 3c). This difference is caused by different behaviors of cationic migration in both samples. For illustrating this point, ex-situ XRD of electrodes of LMNO and LMNPO-V_O at different states of charge are carefully tested (Figure S19). The XRD plots are normalized with 220 peak of Al current collector as a standard. For layered oxides with an $R\bar{3}m$ space group, the intensity ratio of peak 003 to peak 104 (I_{003}/I_{104}) on the XRD plot can directly reflect the degree of cation mixing[39,40]. As shown in Figure 3d, For LMNO, the cation mixing continues to increase from charging to discharging, which is reflected by the continuous decrease of the value for I_{003}/I_{104}. For LMNPO-V_O, cation migration occurs in large quantities during charging, resulting in a sharp decrease in the I_{003}/I_{104} ratio, and when discharging, cations migrate back, resulting in a sharp increase in the I_{003}/I_{104} ratio. Rietveld refinement of the corresponding XRD plots (Figure S20, Table S4) quantify the difference in cation migration between LMNO and LMNPO-V_O, and the results verify the I_{003}/I_{104} ratio.

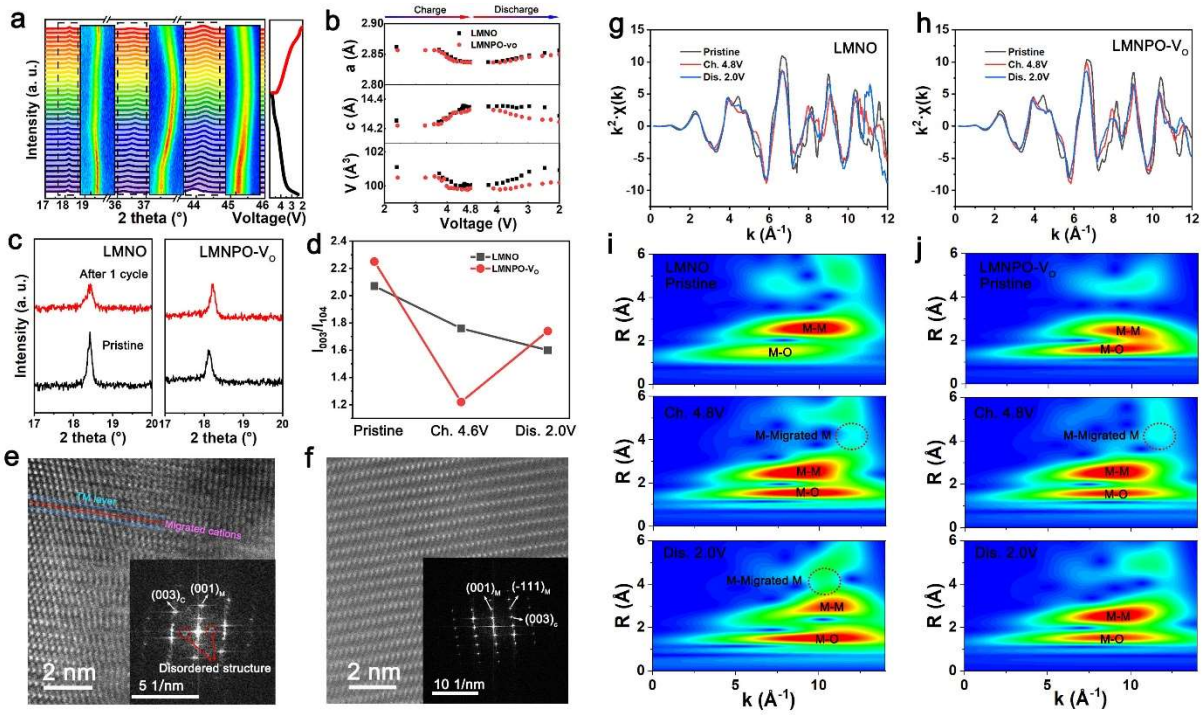

Figure 3. (a) In situ XRD patterns of LMNPO-V_O. (b) The cell parameters change of the LMNO and LMNPO-V_O samples obtained by the Rietveld refinement from the in situ XRD patterns. (c) The in situ XRD plots for LNMO and LNMPO-V_O at pristine and after one cycle. (d) The values of I_{003}/I_{104} in XRD patterns from the ex situ XRD plots for LMNO and LMNPO-V_O in different voltage states. AC-STEM and corresponding FFT images of LMNPO-V_O at 4.8 V charged (e) and 2.0 V discharged (f) states. The EXAFS data of Mn for different electrodes in the k-space of 0-12 $Å^{-1}$ for LMNO (g) and LMNPO-V_O (h). The wavelet transform of Mn K-edge EXAFS spectra for for LMNO (i) and LMNPO-V_O (j).

The Mn cation migration illustrated by AC-STEM are shown in Figure 3e and 3f. Mn atoms are brighter than Li and O atoms for the larger atomic numbers. Combined with the FFT, a large quantity of Mn atoms migrated from the TM slab (cyan line) to the nearest neighbor tetrahedral site in the Li slab (red line) at 4.8V charged state and returned to the original site in the TM slab at 2.0V discharged state.

Figure 3g, 3h plot the extended X-ray absorption fine-structure (EXAFS) data of Mn for different electrodes in the k-space of 0-12 $Å^{-1}$. With charging and discharging, the EXAFS plots of LMNO and LMNPO-V_O show similar changes in the k-space of 0-10 $Å^{-1}$, but different changes in the k-space of 10-12 $Å^{-1}$. This manifests that the low shell coordination variations of Mn in LMNO and LMNPO-V_O are similar, but those for high shell change differently. Wavelet transform of Mn K-edge EXAFS spectra (Figure 3i and 3j) demonstrates that there are

a certain amount of migrating cations in both LMNO and LMNPO-V_O in the 4.8V charged state, which is verified by the signal of M-migrated M shell. After diacharging, this signal disappeares in LMNPO-V_O, but turns more obvious in LMNO. It once again proves the obvious role of LMNPO-V_O in improving the reversible migration of cations.

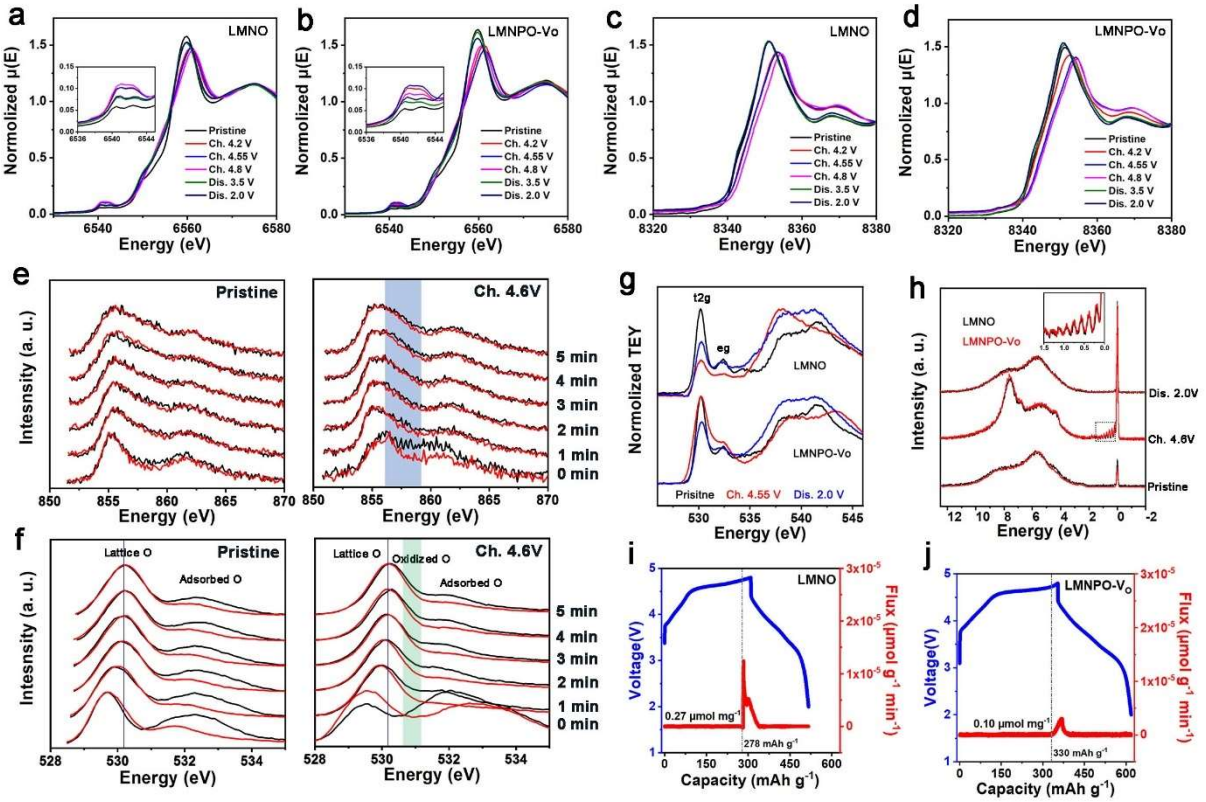

Figure 4. The normalized Mn K-edge spectra of the LMNO (a) and LMNPO-V_O (b) at different states of charge. The insets depict the pre-edge. The normalized Ni K-edge spectra of the LMNO (c) and LMNPO-V_O (d) at different states of charge. (e) The comparison of Ni 2p XPS spectra (e) and O 1s XPS spectra (f) for LMNO (black) and LMNPO-V_O (red) with different Ar^+ etching times. (g) The normalized O pre K-edge soft XAS spectra for LMNO and LMNPO-V_O. (h) The O K-edge RIXS spectra of LMNO and LMNPO-V_O electrodes with the 531eV incident energy. Operando DEMS of LMNO (i) and LMNPO-V_O (j) at 0.1C.

2.4. TM and O redox

Hard X-ray absorption near-edge structure (XANES) of the electrodes at different states of charge is used to explore the charge evolution of bulk TM in LMNO and LMNPO-V_O (Figure 4a, 4b, 4c, 4d). The pre-edge and the edge declare the specific structural information. The pre-edge peak is the forbidden transition of a 1s to 3d orbital for the noncentrosymmetry of the distorted octahedral 3a site in the $R\bar{3}m$ space group, which is sensitive to the valence state[41,42].

The pre-peaks of Mn K-edge do not move obviously in both LMNO and LMNPO-V_O, manifesting the valence states of Mn in two materials do not change much. The position of the white line peak is correlated with electronic properties of Mn cations[43,44]. The changing positions of the white line peak for Mn and Ni K-edges are provided in Figure S21. Upon charging, the position of white line peak for Mn K-edge fot LMNPO-V_O changes more quickly than that in LMNO, manifesting that the kinetics of Mn migration is elevated for LMNPO-V_O. While for Ni K-edge, LMNO and LMNPO-V_O show a similar changing trends of the white line peak position, except that the energy of white line peak for Ni in 2.0V discharged LMNO is higher than that of 2.0V discharged LMNPO-V_O. This means that Ni in LMNPO-V_O is further reduced after discharge, which is helpful to maintain the reversible Ni redox.

XPS combined with Ar^+ etching is used to explore the valence state evolution of transition metal and oxygen in material surface. The valence state of Ni in the surface of 4.6V charged LMNPO-V_O is lower than that of 4.6V charged LMNO, evidenced by the difference of Ni spectra in high binding energies between LMNO and LMNPO-V_O (Figure 4e). As Figure S22 shows, the peaks in Ni 2p spectra of LMNO could not completely return to the pristine state after discharge, manifesting some irreversible degradations in surface of LMNO. While the Ni 2p spectra of pristine and discharged LMNPO-V_O almost coincide, indicating an enhanced Ni redox reversibility. In addition, the Mn spectra of the two materials are also slightly different (Figure S23). Different from the nearly coincident Mn 3s spectra of the two pristine samples, the gaps of the two peaks in Mn 3s spectra of (dis)charged LMNPO-V_O are a little narrower than those of (dis)charged LMNO, reflecting an inhibition of the chemical changes of Mn in charged LMNPO-V_O. The decreasing of changes on Ni/Mn valence state in the surface of LMNPO-V_O is helpful to restrain the deterioration of surface structure.

The O 1s spectra in Figure 4f shows that the O oxidation in the surface of charged LMNPO-V_O is lower than that of charged LMNO. This can be proved in the following aspects. Firstly, the lattice O peaks of 4.6V charged LMNO locate at higher binding energies than those of 4.6V charged LMNPO-V_O, indicating that, after charging, more lattice O escape occurs in LMNO than LMNPO-V_O. Secondly, peaks for oxidized O appear near 530.5 eV in the O 1s spectra of 4.6V charged LMNO, while which is not found in those of 4.6V charged LMNPO-V_O. At the same time, soft X-ray absorption spectroscopy (XAS) also proves this point. The pre-edge peaks of O K-edge spectra at around 530 eV reflect the total d electronic holes in the hybridized O2p-TM3d. Figure 4g shows that the pre-edge peaks of LMNO largely decreases at charging, which may be related to the Mn reduction caused by oxygen redox. Studies have

demonstrated that lattice oxygen oxidation can cause charge transfer from oxygen to TM, accompanied by lattice oxygen escape[45]. The reduction of Mn reduces the density of electronic holes in O2p-Mn3d, thus weakens the O K-edge pre-edge peaks. While due to the inhibition of lattice oxygen redox, the intensity of pre-edge peaks for charged LMNPO-V_O are almost the same with those for pristine LMNPO-V_O. Mn 3s XPS spectra in Figure S23 confirm this inference. Based on the previous studies[46], the peak fitting for O 1s spectra (1 min) at different stats of charge is performed (Figure S24). The peaks at about 529.6 and 532 eV are attributed to the adsorbed oxygen and lattice oxygen (O^{2-}), respectively. The oxidized oxygen is located at 531.2 eV. For the surface of LMNO, an obvious signal of oxidized lattice oxygen has appeared in the spectrum for the 4.3-V charged electrode, but this signal is weakened in the spectrum for the 4.6-V charged electrode, which may be caused by the over-oxidation of lattice oxygen into oxygen gas. As for the surface of LMNPO-V_O, there is no peak of oxidized lattice oxygen in the spectra of the electrodes in 4.3 V and 4.6 V charged states, which confirms the above XAS results.

The O K-edge RIXS spectra of two materials at different voltage states are performed with an incident energy of 531 eV (Figure 4h). The signals around 5.5 eV are attributed to the TM-O hybridization and the O2p orbital. Here the RIXS spectra are normalized based on this peak. The peak at about 7 eV, which appears in the 4.6-V charged electrodes and disappears in the 2.0-V discharged electrodes, is defined as the fingerprint of oxygen redox reaction[47,48]. This fingerprint peak of two materials almost coincide, indicating that the oxygen redox degrees in the bulk of LMNO and LMNPO-V_O are almost the same. In addition, the magnifying region near the elastic peaks at 0 eV shows that the specifics of the vibration peaks. The interval between two vibrated peaks for both materials is 0.2 eV, indicating that the products of local O_2 are generated in both materials[49-51].

Operando differential electrochemical mass spectrometry (DEMS) exhibits the oxygen release in the first charge and discharge process for LMNO and LMNPO-V_O (Figure 4i and 4j). The capacity when O_2 begins to release for LMNPO-Vo is higher than that for LMNO. What's more, the oxygen gas releasing amount is also less (0.1 μmol mg^{-1}) for LMNPO-V_O than LMNO (0.27 μmol mg^{-1}). It indicates that the lattice oxygen escape is largely inhibited in LMNPO-V_O, which can be attributed to the deactivation of surface lattice oxygen and the enhanced covalency of transition metal and lattice oxygen due to P doping for LMNPO-V_O. And the enhanced reversible migrated cations also stabilize the oxdized O species.

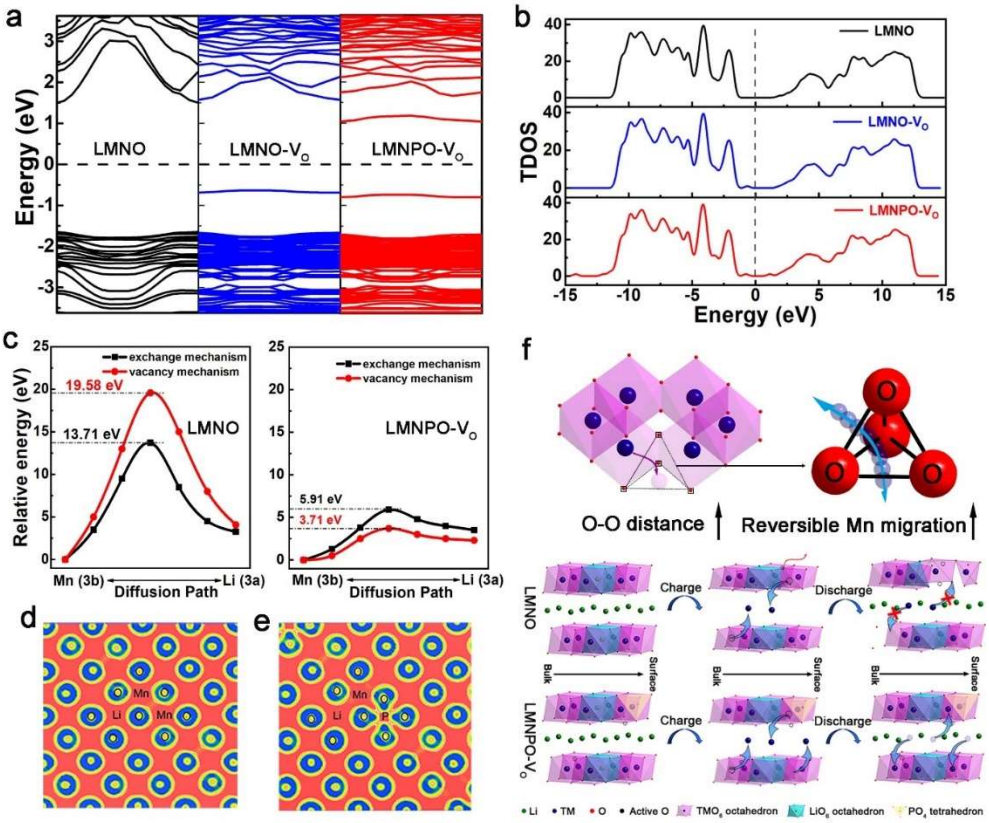

Figure 5. (a) Band structure of LMNO, LMNO-V_O and LMNPO-V_O. (b) TDOS of LMNO, LMNO-V_O and LMNPO-V_O. (c) Mn migration energy barrier from Mn(3b) site to the neighboring Li(3a) site for LMNO and LMNPO-V_O. Electron localization functions (ELF) in (101) plane of LMNO (d) and LMNPO-V_O (e). (f) Mn migration diagram in LMNO and LMNPO-V_O at charging and discharging.

2.5. Theoretical calculations

For revealing the mechanism of the improvements, first-principles calculations based on the density functional theory (DFT) are performed. The calculated band structure for LMNO, LMNO-V_O, and LMNPO-V_O are shown in Figure 5a. It can be seen that the presences of V_O into the lattice add an energy level below the Fermi level of LMNO-V_O and LMNPO-V_O. P doping causes LMNPO-V_O to generate an energy level above the Fermi level. Under the dual action of V_O and P doping, the band gap of LMNPO-V_O has been largely reduced. This is also reflected by total density of state (TDOS) in Figure 5b. It explains the improvements in rate performance and reduction in charge transfer resistance. Figure 5c declares the migration barriers of Mn cation between the metal and lithium sites in LMNO and LMNPO-V_O. Exchange mechanism and the vacancy mechanism, which denote the diffusion mode by exchanging positions between Li and Mn and the diffusion mode of migrating Mn to a Li vacancy, are

calculated. Obvious differences in migration barrier for two materials are exhibited. For LMNO, the energy barriers of Mn migration for the exchange mechanism and the vacancy mechanism are 13.71 eV and 19.58 eV, respectively. While for LMNPO-V_O, the barriers are largely decreased to 5.91 eV and 3.71 eV. The reduction can be explained by the lengthening of the O-O distance from 2.6818(4) to 2.7110(4), which widens the migration channel. The low barrier is favorable to the reversible Mn migration between transition metal site and lithium site. This supports the differences in electrochemical kinetics and voltage hysteresis of LMNO and LMNPO-V_O mentioned above. Increasing the O-O spacing lowers steric hindrance and speeds up the kinetics of cation migration. In this way, the electrochemical kinetics limited by slow cation migration is improved and the rate performance is enhanced, which elevates the contributed discharge capacity by cationic redox at high potentials, thus raises the average discharge voltage of LMNPO-V_O. Meanwhile, more cations migrate to the Li site at charge, and less cations are trapped in Li site at discharge for LMNPO-V_O than LMNO, which improve the structural stability and restrain O release. Electron localization functions in Figure 5d, 5e demonstrate stronger covalent interactions in P-O than that in TM-O. This explains the structural stability enhancement of LMNPO-V_O with P doping.

As the sketch shows in Figure 5f, the mechanism of reversible cation migration is clearly proposed. In the migration path between TMO_6 and LiO_6, the cations are bound to be spatially obstructed by O atoms. Increasing the O-O spacing can reduce steric hindrance and migration barrier, thus facilitating the reversible cation migration. Specifically, for LMNO, Mn cations irreversiblely migrate from TM site to adjacent Li site, resulting in structural degradation. While for LMNPO-V_O, with enlongated O-O, Mn cations migrate from the TM layer to the Li layer in large quantities at charge and then migrate back at discharge, which causes reversible TM_{Li}-V_{TM} antisite in the bulk and thermodynamically enhances the structural reversibility and stabilizes the oxidized O species. Moreover, the spinel-like passivated surface caused by V_O and P doped help restrain the structural degradation and O_2 release by relieving the oxygen redox reactions in surface.

3. Conclusion

In summary, by introducing V_O and P doping into Li-rich oxide, the irreversible TM cation migration and oxygen release are largely restrained. Beneficial changes to the structural characteristics of the oxides are revealed. Combining spectroscopy, diffraction, microscopy, and theoretical calculations, the improving mechanism of LMNPO-V_O is revealed. The combined action of V_O and P doping elongates O-O distance from 2.6818 (4) to 2.7110 (4) Å,

which reduces the steric hindrance, lowers the migration energy barrier and enables a reversible Mn migration. The enhancement of cationic migration kinetics improves the reversibility of cationic redox and elevates the discharge voltage. By increasing the TM_{Li}-V_{TM} antisite at charge and decreasing the trapped cations at discharge, the voltage decay and lattice oxygen escape are simultaneously inhibited. In addition, a strengthened thermodynamic stability of the bulk phase and a reduced lattice oxygen activity in the surface are exhibited because of P doping and surface passivation caused by oxygen vacancies. The cycling stability of the modified cathode material has been enhanced from 85.8 to 98.8% after 200 cycles. The voltage decay rate was restrained from 0.041 to 0.028% per cycle, and the discharge voltage was elevated from 3.387 to 3.512V. The lattice oxygen escape at the initial cycle was relieved from 0.27 to 0.10μmol mg^{-1}. This work demonstrates a new strategy of reducing the steric hindrance for facilitating reversible cation migration and a comprehensive modification involving both bulk and surface, which presents some new insights on resolving the issues of oxygen release and irreversible cation migration in a broad range of oxygen redox cathodes.

4. Experimental Section/Methods

Synthesis of Pristine Materials: The pristine Li-rich materials are synthesized by co-precipitation method: $Li_{1.2}Mn_{0.6}Ni_{0.2}O_2$ (LMNO) and P-doped sample $Li_{1.2}Mn_{0.594}Ni_{0.2}P_{0.006}O_2$ (LMNPO). Initially, the precursor of LMNO is prepared as follows: Na_2CO_3 water solution (50ml, 2M) is added dropwise to the water solution (100ml) containing stoichiometric amounts of $MnSO_4{\cdot}H_2O$ (0.06mol) and $NiSO_4{\cdot}6H_2O$ (0.02mol). After strongly stirring for 9h, the solution is washed with deionized water three times and ethanol two times and dried overnight at 80℃. To synthesize the precursor of LMNPO, we use $MnSO_4{\cdot}H_2O$ (0.0594mol), $NiSO_4{\cdot}6H_2O$ (0.02mol) and $NH_4H_2PO_4$ (0.0006mol) in the same way. Then, the required amount of $LiOH{\cdot}H_2O$ (5% excess) is mixed uniformly into the precursor, and the mixtures are calcined at 500℃ for 5h and 900℃ for 12h.

Hydrazine Treatment. A 1g amount of pristine materials is added into hydrazine (60ml, 2M) and then stirred for 1h. After that, the products are filtered and washed by deionized and ethanol three times and dried overnight at 120℃. The treated samples by hydrazine are named as LMNO-V_O and LMNPO-V_O, respectively.

Material Characterization: The crystalline structures of the as-prepared materials are characterized using an X-ray diffractometer (Rigaku SmartLab, Cu Kα) in the 2θ range of 10°-80°. Neutron diffraction data are collected at China Institute of Atomic Energy with the wavelength of 1.8881 Å. X-ray photoelectron spectroscopy (XPS) analyses are performed on

AXIS Supra with a monochromatic X-ray source (Al Kα). Scanning electron microscopy (SEM, Hitachi SU-8010), Transmission electron microscopy (TEM, Tecnai G2 F30), and An aberration-corrected scanning transmission electron microscope (AC-STEM, JEM ARM200F, JEOL) are performed to investigate the material's morphology and composition. Raman spectra are performed on HORIBA LabRAM Odyssey (532 nm). The defects are detected by an EPR spectrophotometer utilizing a Bruker A300-10/12. X-ray absorption fine structure (XAFS) spectra are collected at the 1W1B beamline of the Beijing Synchrotron Radiation Facility (BSRF, Beijing, China) and soft XAS at the Russian-German Beamline of the synchrotron Bessy II at Helmholtz-Zentrum Berlin, which obtained in electron yield (TEY) modes at room temperature under ultrahigh vacuum (10^{-9} Torr). RIXS data are collected at the PEAXIS beamline of synchrotron BESSY II at Helmholtz-Zentrum Berlin (HZB)[52].

Electrochemical Measurements: Electrochemical performances of the samples are tested in CR2025 coin cells, which are assembled in a glovebox under an Ar atmosphere (H_2O and O_2 content lower than 0.1ppm). Positive electrode tapes are prepared by spreading a slurry containing each one of the electrode materials (80wt%), carbon black Super P (10wt%) and polyvinylidene difluoride (PVDF, 10wt%) mixed in N-methylpyrrolidinone (NMP) solvent on aluminum foil and then dried under vacuum at 120℃ for 12h. After drying, disc electrodes (10mm diameter) are punched and the mass of the active materials loaded on each electrode is close to 2mg. The Galvanostatic intermittent titration technique (GITT) is performed on a battery tester (LAND) between 2.0 and 4.8V. The cyclic voltammograms (CV) and Electrochemical impedance spectroscopy (EIS) are tested on a workstation (Metrohm-Autolab, PGSTAT 302N). Galvanostatic charge-discharge cycling is carried out on a battery tester (NEWARE) between 2.0 and 4.8V (vs Li/Li^+).

Calculation details: The structure optimizations of LMNO and LMNPO-V_O are performed in the frame of density functional theory (DFT) with the program package CASTEP, using the plane-wave ultra-soft pseudopotential (PW-USPP) method and the Perdew-Burke-Ernzerhof (PBE) form of generalized gradient approximation (GGA) exchange-correlation energy functional. The structure optimizations of atomic positions and cell volumes of LMNO and LMNPO-V_O have been carried out employing the Broyden-Fletcher-Goldfarb-Shanno (BFGS) algorithm. In order to make the k-point spacing smaller than $0.04Å^{-1}$, the k-point meshes of 10×10×2 are used over the Brillouin zone (BZ) for LMNO and LMNPO-V_O.

Then, the transition state (TS) searches of Mn migration to the neighboring Li site or Li vacancy in LMNO and LMNPO-V_O are carried out using the program package CASTEP with the

complete LST/QST method. In this method, the linear synchronous transit (LST) maximization is performed, followed by energy minimization in directions conjugating to the reaction pathway to obtain approximated TS. The approximated TS is used to perform quadratic synchronous transit (QST) maximization and then another conjugated gradient minimization is performed. The cycle is repeated until a stationary point was located. The obtained TS is optimized via eigenvector following searching for an energy maximum along with one previously selected normal mode and a minimum along with all other nodes, using Newton–Raphson method.

Supporting Information

Supporting Information is available from the Wiley Online Library or from the author.

Acknowledgements

This work was supported by the National Natural Science Foundation of China (Grant No. 22005302, 11975238 and 11575192), the International Partnership Program (Grant No. 211211KYSB20170060 and 211211KYSB20180020), the Scientific Instrument Developing Project (Grant No. ZDKYYQ20170001), the Strategic Priority Research Program (Grant No. XDB28000000) of the Chinese Academy of Sciences, and the Natural Science Foundation of Beijing (Grant No. 2182082). This work was also supported by the Fundamental Research Funds for the Central Universities, the China Postdoctoral Science Foundation (2020M680648).

Conflict of interest

The authors declare no conflict of interest.

Received: ((will be filled in by the editorial staff))
Revised: ((will be filled in by the editorial staff))
Published online: ((will be filled in by the editorial staff))

References

[1] G. Crabtree, *Science* **2019**, *366*, 422.

[2] Y. Fan, W. Zhang, Y. Zhao, Z. Guo, Q. Cai, *Energy Stor. Mater.* **2021**, *40*, 51.

[3] W. He, W. Guo, H. Wu, L. Lin, Q. Liu, X. Han, Q. Xie, P. Liu, H. Zheng, L. Wang, X. Yu, D. L. Peng, *Adv. Mater.* **2021**, 33, 2005937.

[4] G. H. Lee, V. W. h. Lau, W. Yang, Y. M. Kang, *Adv. Energy Mater.* **2021**, *11*, 2003227.
[5] P. Rozier, J. M. Tarascon, *J. Electrochem. Soc.* **2015**, *162*, A2490.
[6] W. E. Gent, K. Lim, Y. Liang, Q. Li, T. Barnes, S. J. Ahn, K. H. Stone, M. McIntire, J. Hong, J. H. Song, Y. Li, A. Mehta, S. Ermon, T. Tyliszczak, D. Kilcoyne, D. Vine, J. H. Park, S. K. Doo, M. F. Toney, W. Yang, D. Prendergast, W. C. Chueh, *Nat. Commun.* **2017**, *8*, 2091.
[7] J. Chen, W. Deng, X. Gao, S. Yin, L. Yang, H. Liu, G. Zou, H. Hou, X. Ji, *ACS Nano* **2021**, *15*, 6061.
[8] S. Hu, A. S. Pillai, G. Liang, W. K. Pang, H. Wang, Q. Li, Z. Guo, *Electro. Ener. Rev.* **2019**, *2*, 277.
[9] K. Kleiner, B. Strehle, A. R. Baker, S. J. Day, C. C. Tang, I. Buchberger, F.-F. Chesneau, H. A. Gasteiger, M. Piana, *Chem. Mater.* **2018**, *30*, 3656.
[10] Steven G. Rinaldo, Kevin G. Gallagher, Brandon R. Long, Jason R. Croy, Martin Bettge, Daniel P. Abraham, Javier Bareño, Dennis W. Dees, *J. Electrochem. Soc.* **2015**, *162*, A897.
[11] P. Yan, J. Zheng, Z.-K. Tang, A. Devaraj, G. Chen, K. Amine, J.-G. Zhang, L.-M. Liu, C. Wang, *Nat. Nanotechnol.* **2019**, *14*, 602.
[12] Z. Yu, F. Ning, H. Shang, J. Song, T. Yao, Z. Sun, W. Chu, D. Xia, *J. Phys. Chem. C* **2021**, *125*, 16913.
[13] B. Xiao, H. Liu, N. Chen, M. N. Banis, H. Yu, J. Liang, Q. Sun, T. K. Sham, R. Li, M. Cai, G. Botton, X. Sun, *Angew. Chem. Int. Ed.* **2020**, *59*, 14313.
[14] J. Hong, W. E. Gent, P. Xiao, K. Lim, D.-H. Seo, J. Wu, P. M. Csernica, C. J. Takacs, D. Nordlund, C.-J. Sun, K. H. Stone, D. Passarello, W. Yang, D. Prendergast, G. Ceder, M. F. Toney, W. C. Chueh, *Nat. Mater.* **2019**, *18*, 256.
[15] H. Yu, Y.-G. So, Y. Ren, T. Wu, G. Guo, R. Xiao, J. Lu, H. Li, Y. Yang, H. Zhou, R. Wang, K. Amine, Y. Ikuhara, *J. Am. Chem. Soc.* **2018**, *140*, 15279.
[16] B. Xu, C. R. Fell, M. Chi, Y. S. Meng, *Energy Environ. Sci.* **2011**, *4*, 2223.
[17] L. Nation, Y. Wu, X. Liu, M. Chi, Y. Wu, Y. Qi, B. W. Sheldon, *Phys. Chem. Chem. Phys.* **2021**, *23*, 2780.
[18] R. A. House, J.-J. Marie, M. A. Pérez-Osorio, G. J. Rees, E. Boivin, P. G. Bruce, *Nat. Energy* **2021**, *12*, 2975.
[19] P. F. Yan, J. M. Zheng, Z. K. Tang, A. Devaraj, G. Y. Chen, K. Amine, J. G. Zhang, L. M. Liu, C. M. Wang, *Nat. Nanotech.* **2019**, *14*, 602.
[20] Y. Zuo, B. Li, N. Jiang, W. Chu, H. Zhang, R. Zou, D. Xia, *Adv. Mater.* **2018**, *30*, 1707255.

[21] D. Eum, B. Kim, S. J. Kim, H. Park, J. Wu, S. P. Cho, G. Yoon, M. H. Lee, S. K. Jung, W. Yang, W. M. Seong, K. Ku, O. Tamwattana, S. K. Park, I. Hwang, K. Kang, *Nat. Mater.* **2020**, *19*, 419.

[22] Y.-P. Deng, Z.-W. Yin, Z.-G. Wu, S.-J. Zhang, F. Fu, T. Zhang, J.-T. Li, L. Huang, S.-G. Sun, *ACS Appl. Mater. Interfaces* **2017**, *9*, 21065.

[23] X.-D. Zhang, J.-L. Shi, J.-Y. Liang, Y.-X. Yin, J.-N. Zhang, X.-Q. Yu, Y.-G. Guo, *Adv. Mater.* **2018**, *30*, 1801751.

[24] J. Liu, J. Wang, Y. Ni, Y. Zhang, J. Luo, F. Cheng, J. Chen, *Small Methods* **2019**, *3*, 1900350.

[25] Z. Zhu, D. Yu, Y. Yang, C. Su, Y. Huang, Y. Dong, I. Waluyo, B. Wang, A. Hunt, X. Yao, J. Lee, W. Xue, J. Li, *Nat. Energy* **2019**, *4*, 1049.

[26] W. Zhang, Y. Sun, H. Deng, J. Ma, Y. Zeng, Z. Zhu, Z. Lv, H. Xia, X. Ge, S. Cao, Y. Xiao, S. Xi, Y. Du, A. Cao, X. Chen, *Adv. Mater.* **2020**, *32*, 2000496.

[27] X. Ding, D. Luo, J. Cui, H. Xie, Q. Ren, Z. Lin, *Angew. Chem. Int. Ed.* **2020**, *59*, 7778.

[28] Z. Lin, D. Luo, X. Ding, J. Fan, Z. Zhang, P. Liu, X. Yang, J. Guo, S. Sun, *Angew. Chem. Int. Ed.* **2020**, *59*, 23061.

[29] T. Wu, X. Liu, X. Zhang, Y. Lu, B. Wang, Q. Deng, Y. Yang, E. Wang, Z. Lyu, Y. Li, Y. Wang, Y. Lyu, C. He, Y. Ren, G. Xu, X. Sun, K. Amine, H. Yu, *Adv. Mater.* **2021**, *33*, 2001358.

[30] T. Nakamura, K. Ohta, X. Hou, Y. Kimura, K. Tsuruta, Y. Tamenori, R. Aso, H. Yoshida, K. Amezawa, *J. Mater. Chem. A* **2021**, *9*, 3657.

[31] Z. Ye, B. Zhang, T. Chen, Z. Wu, D. Wang, W. Xiang, Y. Sun, Y. Liu, Y. Liu, J. Zhang, Y. Song, X. Guo, *Angew. Chem. Int. Ed.* **2021**, *60*, 23248.

[32] J. He, A. Missyul, W. Hua, G. Melinte, C. Das, A. Tayal, T. Bergfeldt, S. Mangold, X. Liu, J. R. Binder, M. Knapp, H. Ehrenberg, S. Indris, B. Schwarz, J. Maibach, *J. Mater. Chem. A* **2020**, *9*, 264.

[33] B. Li, H. Yan, J. Ma, P. Yu, D. Xia, W. Huang, W. Chu, Z. Wu, *Adv. Funct. Mater.* **2014**, *24*, 5112.

[34] R. Yu, M. N. Banis, C. Wang, B. Wu, Y. Huang, S. Cao, J. Li, S. Jamil, X. Lin, F. Zhao, W. Lin, B. Chang, X. Yang, H. Huang, X. Wang, X. Sun, *Energy Stor. Mater.* **2021**, *37*, 509.

[35] K. Nakayama, R. Ishikawa, S. Kobayashi, N. Shibata, Y. Ikuhara, *Nat. Commun.* **2020**, *11*, 4452.

[36] G. Assat, D. Foix, C. Delacourt, A. Iadecola, R. Dedryvère, J.-M. Tarascon, *Nat. Commun.* **2017**, *8*, 2219.

[37] D. Ye, G. Zeng, K. Nogita, K. Ozawa, M. Hankel, D. J. Searles, L. Wang, *Adv. Funct. Mater.* **2015**, *25*, 7488.
[38] Q. Li, D. Ning, D. Zhou, K. An, G. Schuck, D. Wong, W. Kong, C. Schulz, G. Schumacher, X. Liu, *Chem. Mater.* **2020**, *32*, 9404.
[39] Y. Y. Hu, Z. Z. Qin, J. Pei, B. W. Cong, X. Yang, G. Chen, *Chemelectrochem* **2020**, *7*, 246.
[40] J. Zhang, D. Zhou, W. Yang, J. Yang, L. Sun, G. Schumacher, X. Liu, *J. Electrochem. Soc.* **2019**, *166*, A4097.
[41] H. Koga, L. Croguennec, M. Ménétrier, P. Mannessiez, F. Weill, C. Delmas, S. Belin, *J. Phys. Chem. C* **2014**, *118*, 5700.
[42] W. S. Yoon, M. Balasubramanian, K. Y. Chung, X. Q. Yang, J. McBreen, C. P. Grey, D. A. Fischer, *J. Am. Chem. Soc.* **2005**, *127*, 17479.
[43] E. M. Erickson, H. Sclar, F. Schipper, J. Liu, R. Tian, C. Ghanty, L. Burstein, N. Leifer, J. Grinblat, M. Talianker, J.-Y. Shin, J. K. Lampert, B. Markovsky, A. I. Frenkel, D. Aurbach, *Adv. Energy Mater.* **2017**, *7*, 1700708.
[44] K. Luo, M. R. Roberts, R. Hao, N. Guerrini, D. M. Pickup, Y.-S. Liu, K. Edström, J. Guo, A. V. Chadwick, L. C. Duda, P. G. Bruce, *Nat. Chem.* **2016**, *8*, 684.
[45] D. Dixon, S. Mangold, M. Knapp, H. Ehrenberg, A. Bhaskar, *Adv. Energy Mater.* **2021**, *11*, 2100479.
[46] P. E. Pearce, A. J. Perez, G. Rousse, M. Saubanère, D. Batuk, D. Foix, E. McCalla, A. M. Abakumov, G. Van Tendeloo, M.-L. Doublet, J.-M. Tarascon, *Nat. Mater.* **2017**, *16*, 580.
[47] U. Maitra, R. A. House, J. W. Somerville, N. Tapia-Ruiz, J. G. Lozano, N. Guerrini, R. Hao, K. Luo, L. Jin, M. A. Perez-Osorio, F. Massel, D. M. Pickup, S. Ramos, X. Lu, D. E. McNally, A. V. Chadwick, F. Giustino, T. Schmitt, L. C. Duda, M. R. Roberts, P. G. Bruce, *Nat. Chem.* **2018**, *10*, 288.
[48] J. Xu, M. Sun, R. Qiao, S. E. Renfrew, L. Ma, T. Wu, S. Hwang, D. Nordlund, D. Su, K. Amine, J. Lu, B. D. McCloskey, W. Yang, W. Tong, *Nat. Commun.* **2018**, *9*, 947.
[49] J. Zhang, Q. Zhang, D. Wong, N. Zhang, G. Ren, L. Gu, C. Schulz, L. He, Y. Yu, X. Liu, *Nat. Commun.* **2021**, *12*, 3071.
[50] R. A. House, J. J. Marie, J. Park, G. J. Rees, S. Agrestini, A. Nag, M. Garcia-Fernandez, K. J. Zhou, P. G. Bruce, *Nat. Commun.* **2021**, *12*, 2975.
[51] R. Sharpee, R. A. House, M. J. Clarke, D. Förstermann, J.-J. Marie, G. Cibin, K.-J. Zhou, H. Y. Playford, P. G. Bruce, M. S. Islam, *J. Am. Chem. Soc.* **2020**, *142*, 21799.

[52] C. Schulz, K. Lieutenant, J. Xiao, T. Hofmann, D. Wong, K. Habicht, *J. Synchrotron Rad.* **2020**, *27*, 238.